RSC Advances

PAPER

View Article Online
View Journal | View Issue

Cite this: *RSC Adv.*, 2024, **14**, 31966

A novel porous interbody fusion cage modified by microarc oxidation and hydrothermal treatment technology accelerate osseointegration and spinal fusion in sheep†

Jiang Sun,‡[abc] Shan-Shan Liu,‡[abc] Da Zou,[abc] Ren-Hua Ni,[abc] Chong-Bin Wei,[d] Hao Wang[d] and Wei-Shi Li *[abc]

The clinical outcome of spinal fusion surgery is closely related to the success of bone fusion. Nowadays, the interbody cage which is used to replace the disc for spinal fusion is expected to have biological activity to improve osseointegration, especially for the aging and osteoporotic patients. Here, through micro-arc oxidation and hydrothermal treatment (MAO + HT), a bioactive CaP coating with micro/nano multilevel morphology was developed on 3D printed Ti6Al4V alloy then verified *in vitro* and in sheep anterior cervical decompression fusion model systematically. *In vitro* studies have confirmed the positive effects of characteristic micro/nano morphology and hydrophilicity of the coating formed after surface treatment on the adhesion, proliferation, and osteogenic differentiation of osteoblast precursor cells. Furthermore, the MAO + HT treated interbody cage showed a closer integration with the surrounding bone tissue, improved kinetic stability of the implanted segment, and significantly reduced incidence of fusion failure during the early postoperative period, which indicated that such a surface modification strategy is applicable to the biomechanical and biological microenvironment of the intervertebral space.

Received 30th November 2023
Accepted 25th August 2024

DOI: 10.1039/d3ra08185k

rsc.li/rsc-advances

1 Introduction

Lumbar fusion often remains the last treatment option for degenerative disc disease, spondylolisthesis, trauma, tumor reconstruction and scoliosis which has been the case for decades.[1] Over 400 000 spinal fusion surgeries are performed in the United States annually, with estimated costs exceeding $33 billion which are reported to be among the top 3 costly procedures for the Medicare system.[2] In spinal surgery, once the disc is completely removed, a cage is placed in the interspace to replace the disc for the spinal fusion.[3] Since its first use by Bagby in 1988,[4] interbody cages have become a highly successful means of achieving fusion, being associated with less postoperative pain, shorter hospital stay, fewer complications and higher rates of fusion than bone graft only spinal fusion.[5] Polyetheretherketone (PEEK) and titanium-alloy interbody cages are traditionally used. Nowadays, additive manufacturing (AM) technology was introduced to simulate natural bone tissue in terms of structural and biomechanical properties, thereby reducing stress shielding and improving osteoconductivity as well as the metabolic efficiency of nutrients. Some *in vivo* studies and case reports have reported that 3D printed titanium alloy cage can accelerate osseointegration and improve the stability of fusion segments compared with traditional solid titanium alloy and PEEK.[6–10] However, complications such as vertebral endplate cyst formation and cage subsidence (8/6 in 36 cases) were still reported in the 3D printed tested group,[10] suggesting that the intrinsic osseointegration of fusion device still needs to be further improved to cope with the needs of clinical, especially the elderly population with decreased bone quality.

Most cases of spinal fusion failure can be attributed to layer of fibrous connective tissue that grows between the bone and the implant,[11] which is now well accepted that can be avoided by optimizing the micro- and nanoscale topography and chemical composition of the implant surface. Except through physical behavior just like increasing friction, aiding in initial fixation and limiting micromotion,[12] suitable surface properties can benefit intervertebral fusion intervertebral fusion by reducing the probability of aseptic inflammation, promoting adsorption of selective proteins such as vitronectin and fibronectin, stimulating

[a]*Peking University Third Hospital, Beijing, 100191, China. E-mail: sjdoctor@pku.edu.cn; 1039165305@qq.com; zd_puth@163.com; tiffanyni@126.com; puh3liweishi@163.com*

[b]*Engineering Research Center of Bone and Joint Precision Medicine Department of Orthopedics, Beijing, 100191, China*

[c]*Beijing Key Laboratory of Spinal Disease Research, Beijing, 100191, China*

[d]*Beijing AKec Medical Co., Ltd, Beijing 102200, China. E-mail: chongbin.wei@ak-medical.net; hao.wang@ak-medical.net*

† Electronic supplementary information (ESI) available. See DOI: https://doi.org/10.1039/d3ra08185k

‡ Jiang Sun and Shan-Shan Liu contribute equally to this manuscript and are considered as co-first authors.

osteogenic cell migration and differentiation.[13,14] Prior researchers have successfully developed coatings covered the entire surfaces of porous titanium displaying promising osteogenic and osteointegration effects,[15] through the use of anodization, microarc oxidization (MAO), grit blast, acid-alkali treatments and electrodeposition.[16–19] Among those, microarc oxidation is a relatively simple and reliable technique, after treatment, there is not only the formation of porous oxide layer structures on the Ti alloy surfaces, but also the incorporation of abundant calcium and phosphorus chemical elements. The characteristics of the coatings can be adjusted by changing the voltage, current, electrolyte composition, and process duration.[20,21]

In recent years, researchers have been exploring new rapid surface modification techniques to modify MAO coatings in order to form more bioactive surfaces, such as hydrothermal treatment (HT),[22–27] alkali treatment,[28,29] and sol–gel method.[30,31] Titanium alloys treated with the above techniques often need to be tested for biocompatibility and osteoinductivity to determine whether the obtained surface characteristics, such as roughness and chemical composition, are conducive to bone repair.[20,25,27,32–35] For instance, Huang *et al.* found the MAO-HT-fabricated coating exhibits enhanced hydrophilicity, fibronectin adsorption and initial MG-63 cell attachment compared with single-scale surface topography MAO-fabricated coating.[36] The above reports are often based on the *in vitro* experiments or the performance of materials applied to rodent bone defect models. However, such results are not necessarily applicable to interbody fusion. First, the physiological mechanical loads are mainly oriented parallel to the longitudinal axis of the limbs, yet the stress directions and distribution of the cage in the intervertebral space change accompanied by the spine segmental motion. For example, *in vivo* pressures in the nucleus are between 460 and 1330 kPa in the seated position, 500 and 870 kPa in the standing position, and 91 and 539 kPa when lying either prone or supine.[37] Second, interbody fusion cage is in direct contact with the bony endplate of the vertebral body and integrated with upper and lower endplates by endochondral ossification. In contrast, bone defect repair scaffolds often come into contact with periosteum, cortical bone, and large area cancellous bone, providing a more favorable physiological environment for bone fusion. Thus, whether 3D printed titanium alloy fusion cage after MAO-HT treatment has advantages in the special physiological environment of intervertebral space is still unclear.

In this study, we aimed to develop a characteristic morphology and chemical composition on the surface of 3D printed titanium with good cytocompatibility and osteogenesis induction ability *via* MAO + HT treatment. Further, cages with the bioactive coating described above will be implanted into a sheep anterior cervical discectomy and fusion (ACDF) model to systematically evaluated its ability to promote intervertebral fusion compared with untreated titanium alloy interbody cages.

2 Materials and methods

2.1. AM and surface treatment of porous Ti6Al4V

All samples were prepared using an EBM Q10 Plus (Arcam AB, Sweden). The porous structure was designed based on a bionic trabecular structure unit cell using CAD software. The porous Ti6Al4V scaffold was printed with a pore size of ~600 μm, strut diameter of ~400 μm, and porosity of ~70%. According to previous studies,[38] the interbody cages was fabricated to a rectangular design with an outer dimension of 12 mm × 10 mm × 5–6 mm in the animal experiments (ESI Fig. 1†). Samples were sequentially washed by acetone, acid pickled and ethanol in ultrasonic cleaner (KQ-250D, China). For MAO treatment, the porous Ti6Al4V alloy were used as an anode, and a stainless plate was used as a cathode in an electrolytic bath. The electrolytes were composed of 0.065 M Ca $(CH_3COO)_2 \cdot H_2O$, 0.03 M NaH_2PO_4, 0.065 M EDTA-2Na, and 0.5 M NaOH. The reaction parameters are set as follows: 450 V working voltage, 500 Hz pulse frequency, 10% duty ratio and 10 min reaction time. Maintain the bath temperature below 40 °C with water cooling. After ultrasonically rinsed with distilled water for 5 min, MAO treated samples were treated in a sodium hydrate solution (NaOH, 0.01 M). In detail, the sodium hydrate solution was heated up to 80 °C, with a heating rate of 5 °C min^{-1}. The temperature was kept for 12 hours. Subsequently, the solution was naturally cooled to room temperature. The MAO + HT treated samples were gently rinsed with deionized water and then dried in ambient atmosphere. After the hydrothermal treatment of the titanium alloy implant samples, subsequent cleaning is required to remove NaOH residues. The cleaned samples are placed in a 50 ml centrifuge tube with 20 ml of pure water for 30 minutes of ultrasonic cleaning.

2.2. Characterization of MAO-HT coating

The macro-, micro-, and nanostructure of MAO + HT treated surface were acquired by scanning electron microscopy (SEM; Hitachi, Regulus 8100, Japan) at 0.1k, 1k and 20k magnifications. The samples were fixed on a tray with conductive glue then sprayed using an ion sputter coater (Hitachi, E-1010, Japan) before testing in order to enhance the conductivity of the material. The water contact angle of each surface was measured to identify their wettability (Kino, SCA20, USA). The shape of the 1 μL drops of deionized water taken at three locations per sample were recorded using software to calculate the water contact angle. To reduce the influence of macroscopic porosity on contact angle measurements, disc samples were used for this test. The crystallinity of the coating was analyzed using X-ray diffraction (XRD; Bruker, D8 Focus, Germany) equipped with a Cu-Kα radiation source. The setting parameters were as follows: the incident beam wavelength (λ) was 1.54 Å, the scanning range was 10–80° and the operating current was 50 mA. The surface chemistry of 3D printed scaffold after the MAO + HT treatment was acquired using X-ray photoelectron spectroscopy (XPS; Kratos, AXIS UltraDLD, Japan). XPS results were analyzed on the basis of binding energies of Ca2p, P2p and O1s to evaluate the chemical environment and oxidation states of the respective elements on the surface.

2.3. *In vitro* cell experiments

Passage 3 human bone marrow mesenchymal stem cells (hBMSCs, LONZA, Switzerland) were cultured into cylindrical

(∅3 × 6 mm) samples to evaluate the cytocompatibility and osteogenic properties of MAO + HT and untreated titanium alloy scaffold.

2.3.1. Cell culture. The cells were resuspended with α-minimum essential medium (α-MEM, Gibco, USA) containing 10% fetal bovine serum (FBS, Gibco, USA), 100 U per mL penicillin and 100 mg per mL streptomycin, then seeded at a density of 2×10^5 cells per mL on samples contained in 48-well plates. After a 4 hour incubation period, 800 μL of culture medium was added each well.

2.3.2. Cell proliferation activity. Cell viability was determined *via* LIVE/DEAD Viability/Cytotoxicity Kit (Thermo Fisher, USA) and CCK8 assay (Dojindo, Japan). Following 24 h incubation, the samples were washed with PBS and transferred to a new 48-well plate. The LIVE/DEAD reagents were added to each well and the culture plates were incubated at RT for 30 min, protected from light. Finally, fluorescent signals were visualized under a confocal laser microscope (CLSM, Leica, Germany). In the CCK8 test, CCK8 reagents were added to each well and incubated for 2 hours at 37 °C after 3, 7, and 14 days of culture. Cells seeded in wells without sample were used as the controls. The optical density (OD) of CCK-8 was measured at 450 nm reflecting cell viability.

2.3.3. Cell adhesion. The hBMSCs morphology on sample was evaluated using DAPI (Beyotime, China) and FITC phalloidin (Cytoskeleton, USA). Following 24 h incubation, the samples were washed with PBS and transferred to a new 48-well plate. Cells adhered onto scaffolds were fixed with 4% paraformaldehyde for 15 min at room temperature. Then FITC phalloidin was added to stain F-actin, and DAPI stain nucleus. The stained cells were observed through a CLSM.

2.3.4. ALP activity. After 7 and 14 days of culture, cells adhered onto scaffolds were lysed, the supernatants were collected after centrifugation, and the total protein content was determined by a BCA assay. For ALP activity analysis, the protein was incubated with *p*-nitrophenyl phosphate (Beyotime, China) at 37 °C for 15 minutes. Calculate the ALP activity level based on the absorbance at 405 nm expressed in nanomoles of produced *p*-nitrophenol per min per mg of protein (nmol per min per mg protein) normalized to the BCA results.

2.4. Animal experiment

2.4.1. Operative procedure. The sheep cervical motion segment has been regarded as an ideal experimental model for analogy of human cervical motion segment due to the biomechanical similarity.[39] The experiment was approved by the Peking University Institutional Review Board Office (LA2022558). A total of 24 female Small Tailed Han sheep (1 year old, about 50 kg) were performed the anterior cervical decompression and fusion at C2–C3 and C3–C4. The sheep was bound on the operating table in a fixed supine position after anesthesia was induced by injection of 2 mg per kg propofol. The neck area was shaved and strictly disinfected by 70% ethyl alcohol. Starting from 2 cm below the thyroid cartilage, a 10 cm long median longitudinal incision was made in the skin of the neck. The trachea and esophagus are shifted to one side and the fascia, ligament, and cervical longus muscle are separated layer by layer along the midline until the cervical vertebral body is exposed. In each disc level, a complete discectomy was performed, then 3D printed porous interbody cage (untreated or MAO + HT) was placed in the interspace to replace the disc randomly. After implantation, an anterior titanium plate and screws system were used to stabilize cervical vertebrae. 12 experimental animals were sacrificed with diazepam and KCl overdose at 3 and 6 months after operation, and their spinal columns were harvested, including segments C1–C5 containing interbody cages with all ligamentous structures. 12 sheep were programmed for radiographic and histological analysis, and the other 12 were used for biomechanical assessment.

2.4.2. Micro-CT measurement. Peri-implant osseointegration was visualized by Micro-CT device (Siemens INVEON MM, Germany). The scanning parameters were as follows: 70 kV and 400 μA in the X-ray tube, 13 μm scan resolution, and 400 ms exposure time. From each specimen, a 500 μm high cylinder was selected as region of interest (ROI) centered at the interface between the fusion cage and the endplate, the upper and lower end plates are calculated separately. The osseous integration of the cages to the vertebral endplates was graded as follows partial based on previous studies:[10] (0: no fusion, bone ingrowth in less than 20% of ROI, 1: partial fusion, bone ingrowth in 20–80% of ROI with or without bridging bone formation, 2: full fusion, bone ingrowth in more than 80% ROI accompanied by wide bridging bone formation). The reconstructed 3D images were processed by the Inveon Acquisition Workplace (Siemens, INVEON MM, Germany), which in turn were used to analyze trabecular parameters including bone volume over total volume (BV/TV), trabecular number (Tb.N), trabecular thickness (Tb.Th) and trabecular separation (Th.Sp).

2.4.3. Sequential fluorescent labeling. To analyse the osseointegration efficiency and direction around the interbody cages, *in vivo* sequential fluorescence labelling was performed.[40] Fluorescent staining agents calcein green (10 mg kg^{-1}, Sigma, USA) and xylenol orange (90 mg kg^{-1}, Sigma, USA) were injected intravenously at 10 and 30 days before sacrifice to label the newly formed bone. The fluorescence signals emitted were detected at 488 nm (calcein) or 543 nm (xylenol orange). The mineral apposition rate (MAR) was calculated using the distance between dye labeling divided by the number of interval days.

2.4.4. Histological analysis. The surgical vertebral segment samples were fixed in 4% formaldehyde for 4 days at room temperature followed by the removal of excess muscle and ligament. The embedding and polymerization processes of the monosegments were carried out in methyl methacrylate (MMA, Technovit 9100 New, Germany) after dehydration by ethanol gradient (50–70–95–100%). Using a special diamond band saw (Exakt 310, Germany), the MMA blocks were cut into 150 μm thick sections, then ground and polished to a final thickness of 100 μm for histological analysis. The methylene blue acid fuchsin (Solarbio, China) and modified Goldner trichrome staining (Solarbio, China) method was used to distinguish the neo-generated tissues around the interbody cages as well as within the porous structures according to the product manual.

2.4.5. SEM/EDS analysis. The MMA sections were sputtered with gold using an ion sputter coater, then observed under an SEM (Hitachi S-4800, Japan) equipped with an Energy Dispersive Spectrometer (EDS, Bruker QUANTAX, Germany) to characterized the structure of material–bone interface as well as the elemental compositions and cross-sectional mappings of Ti, phosphorous (P), calcium (Ca), carbon (C), oxygen (O). The working distance and accelerating voltage were 10 mm and 15 kV.

2.4.6. Biomechanical analysis. The operated spinal motion segments were explanted immediately following sacrifice. The extra muscles were eliminated, while ligamentous structures were preserved. Both ends of the spinal motion segment were then fixed in stainless steel molds by bone cement. Keep the specimen moist during the test by spraying saline every 5 minutes. The biomechanical experiment procedure and steps refer to our previous work.[41] Pilot markers were immobilized to the lateral aspect of the vertebral bodies of C2 and C3, to track their respective segmental range of motion (ROM), which was measured and analyzed using NDI Optotrak Certus, a 3D movement measuring system (Ontario, Canada). Preconditioning each sample for three loading cycles with a torque variation between 2 Nm and −2 Nm to minimize viscoelastic effects. Then, starting from a neutral position, each specimen was tested in three different directions of motion in the order of extension–flexion (*i.e.*, anterior–posterior translation, lateral bending, and axial rotation while keeping the displacement under control between angles corresponding to the moments between 2 NM and −2 NM as determined in the previous viscoelasticity mitigation step). Three-dimensional coordinates of the marker pilot markers were recorded. The accuracy of the

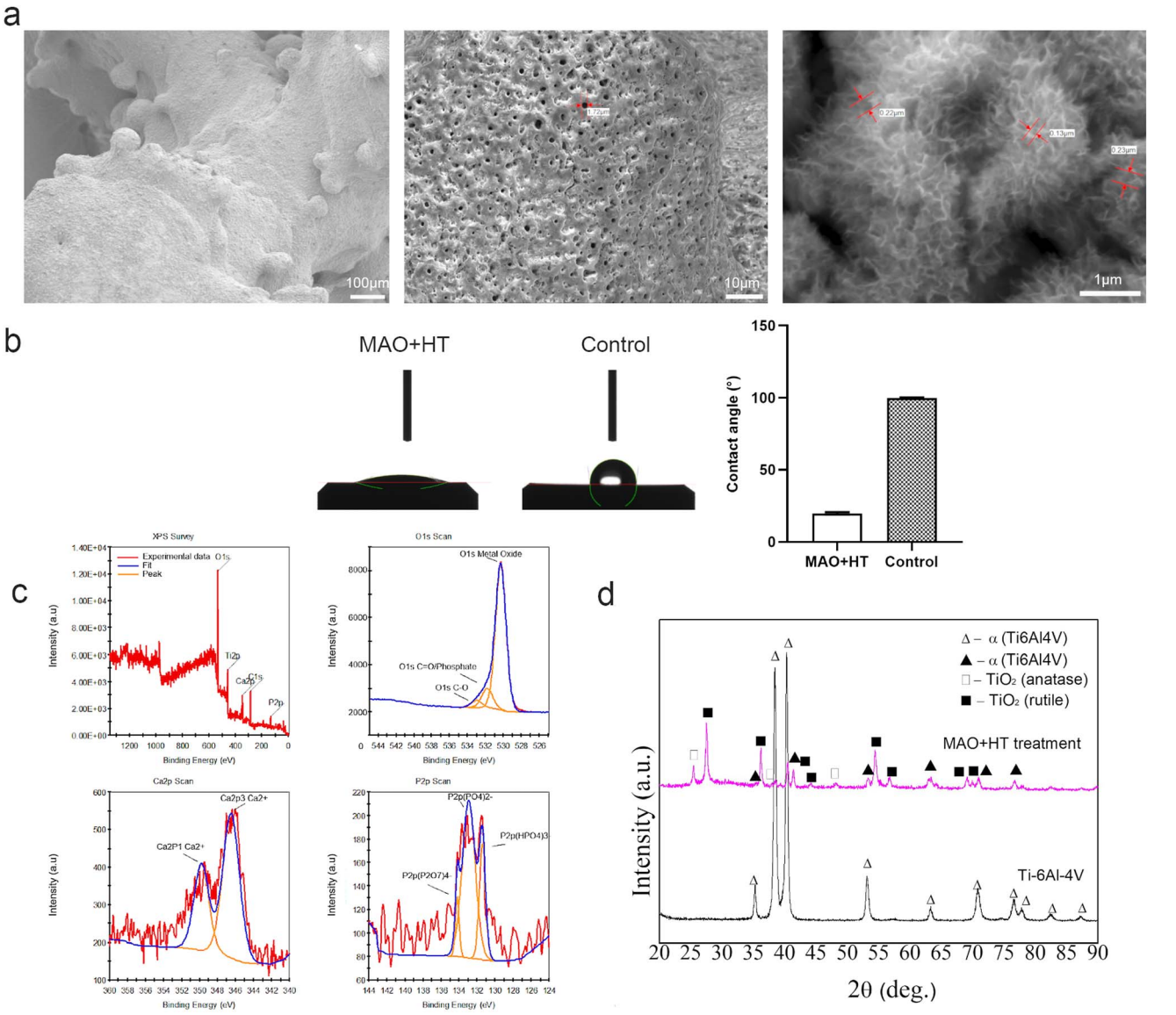

Fig. 1 Representative macroscale, microscale and nanoscale SEM images of MAO + HT treated surface at 0.1k, 1k and 20k magnifications, red arrows refer to the diameter of characteristic structural units at different magnifications (a); representative images and quantitative analysis of the contact angle test, $n = 3$ in each group (b); XPS survey and high-resolution spectra at the O1s, Ca2p and P2p core-level energy region of the MAO + HT treated surfaces (c); XRD patterns before and after surface treatment (d).

NDI system used for rigid body displacement measurement is 0.01 mm.

2.5. Statistical analysis

Statistical analysis was performed on SPSS 17.0 software (SPSS Institute Inc., USA), using independent sample *t*-test and one-way analysis of variance (ANOVA). All experiment data were expressed as means ± standard deviations (SD) and any of $p < 0.05$ (indicated as *), $p < 0.01$ (indicated as **), $p < 0.001$ (indicated as ***) was considered to be significant.

3 Results

3.1. *In vitro* results

3.1.1. Materials characterization. Representative SEM image under 1k magnification shows the surface of the MAO-treated scaffold was covered by numerous evenly distributed crater-like micro porous structures with various pore sizes around 0.5–5 μm (Fig. 1a). In contrast, significantly different unique hemispheric rosette-like "clumps" (3–5 μm in diameter) appeared on the surfaces under 20k magnification, and each "clump" consists of numerous "petals" (0.1–0.3 μm in diameter). The wettability of 3D printed scaffold surface was shown in Fig. 1b. The contact angle results for the untreated and MAO + HT treated samples were 99.90 ± 0.44° and 19.75 ± 0.80°. Fig. 1c shows the XPS survey spectra and high-resolution spectrum of the sample surface. The surface products are mainly composed of Ca, Ti, P and O, and the high oxygen content on the surface is due to surface oxidation. According to the high-resolution spectrum of Ca_{2p} and P_{2p} on the sample surfaces, the Ca_{2p} peaks of Ca^{2+} are well fitted at 350 eV and 347 eV, and the P_{2p} peaks of the surface products are well fitted with three contributions at 135 eV, 133 eV and 131 eV, which are determined as $(P_2O_7)^{4-}$, $(PO_4)^{2-}$ and $(HPO_4)^{3-}$. According to the standard binding peak of the reference compound, the coatings developed by MAO + HT treatment contains $Ca_2(P_2O_7)$, $Ca(PO_4)$, $Ca_3(HPO_4)_2$, which suggests that a calcium-phosphorus rich layer has been successfully incorporated into the implant surface. The XRD pattern of the 3D printed porous Ti6Al4V alloy before and after MAO + HT treatment is shown in Fig. 1d. Only the diffraction peak of the HCP structure (α phase) was detected in the untreated Ti6Al4V alloy. However, after MAO + HT treatment, the surface structure changed significantly. In addition to the α phase, the phases of anatase TiO_2 and rutile TiO_2 with obvious diffraction peaks were detected. Meanwhile, compared with that before MAO + HT treatment, the diffraction peak intensity of α phase after MAO + HT treatment is weakened, which indicates that MAO + HT treatment leads to the decrease of texture intensity of the alloy.

3.1.2. *In vitro* cytocompatibility of MAO + HT coating. Through representative pictures of live (green) and dead (red)

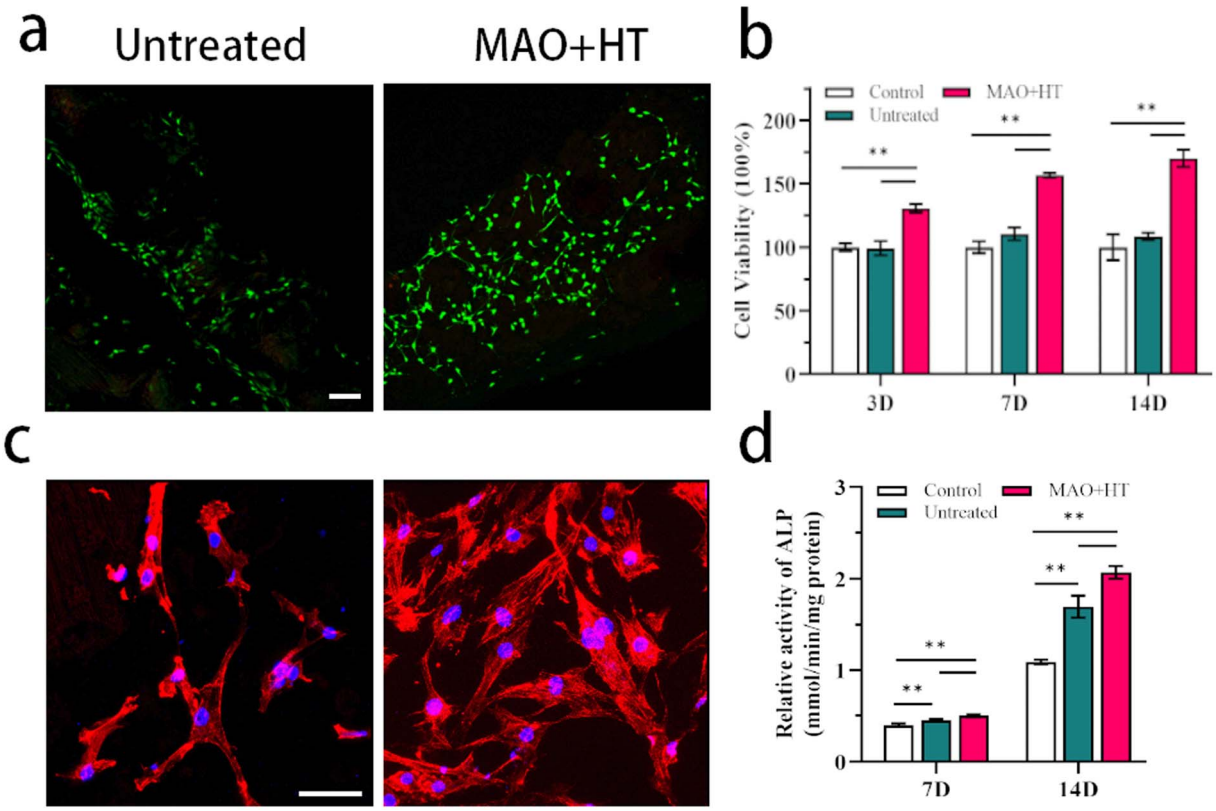

Fig. 2 *In vitro* cytocompatibility and osteogenic properties of different surface condition: (a) Live/Dead assay (green, live cell; red, dead cell) of hBMSCs seeded on scaffolds for 24 h; (b) CCK-8 assay after culturing for 3, 7 and 14 days; (c) CLSM images of cytoskeleton (phalloidin, red) and nuclei (DAPI, blue) of hBMSCs seeded on scaffolds for 24 h; (d) quantification of ALP activity relative to total protein after culturing for 7 and 14 days, the size bar represents 100 μm.

cells adhered onto the scaffold surface (Fig. 2a), more uniformly distributed live cells can be observed on the MAO + HT coatings. However, no dead cells were detected in both groups. CCK8 assays indicated proliferative capacity of hBMSCs on different surface conditions. MAO + HT coatings were confirmed to significantly stimulate cell viability, with 130.67 ± 3.40 at 3 days, 156.82 ± 1.90 at 7 days and 170.13 ± 6.75 at 14 days ($p < 0.01$). In comparison, cell proliferation on untreated surface was similar to the blank control at 3 and 14 days (Fig. 2b). Fig. 2c shows the cytoskeletal morphology of cells adhered onto the two kinds of scaffolds surface. The hBMSCs on MAO + HT treated scaffolds tightly grasp to the scaffold surface *via* lamellipodia and filopodia, exhibited a widespread and flattened shape. Conversely, cells on the untreaded surface displayed poor cell spreading situation with obvious narrowly elongated morphologies and cell shrinkage.

3.1.3. *In vitro* osteogenic properties of MAO + HT coating. As an early marker of MSC differentiation in protein level, ALP activity was measured at 7 and 14 days to assess the osteogenic differentiation potential of hBMSCs seeded on the two kinds of material surfaces (Fig. 2d). Cells cultured on MAO + HT coatings (0.50 ± 0.02 mmol per min per mg protein) exhibited significantly higher ALP activity than that on untreated surface (0.45 ± 0.01 mmol per min per mg protein) at 7 days ($p < 0.01$). This difference was amplified to 2.07 ± 0.07 mmol per min per mg protein verse 1.70 ± 0.12 mmol per min per mg protein at 14 days ($p < 0.01$).

3.2. *In vivo* results

3.2.1. Micro-CT analysis. Representative 2D and 3D micro-CT images of cages and the upper and lower endplates are

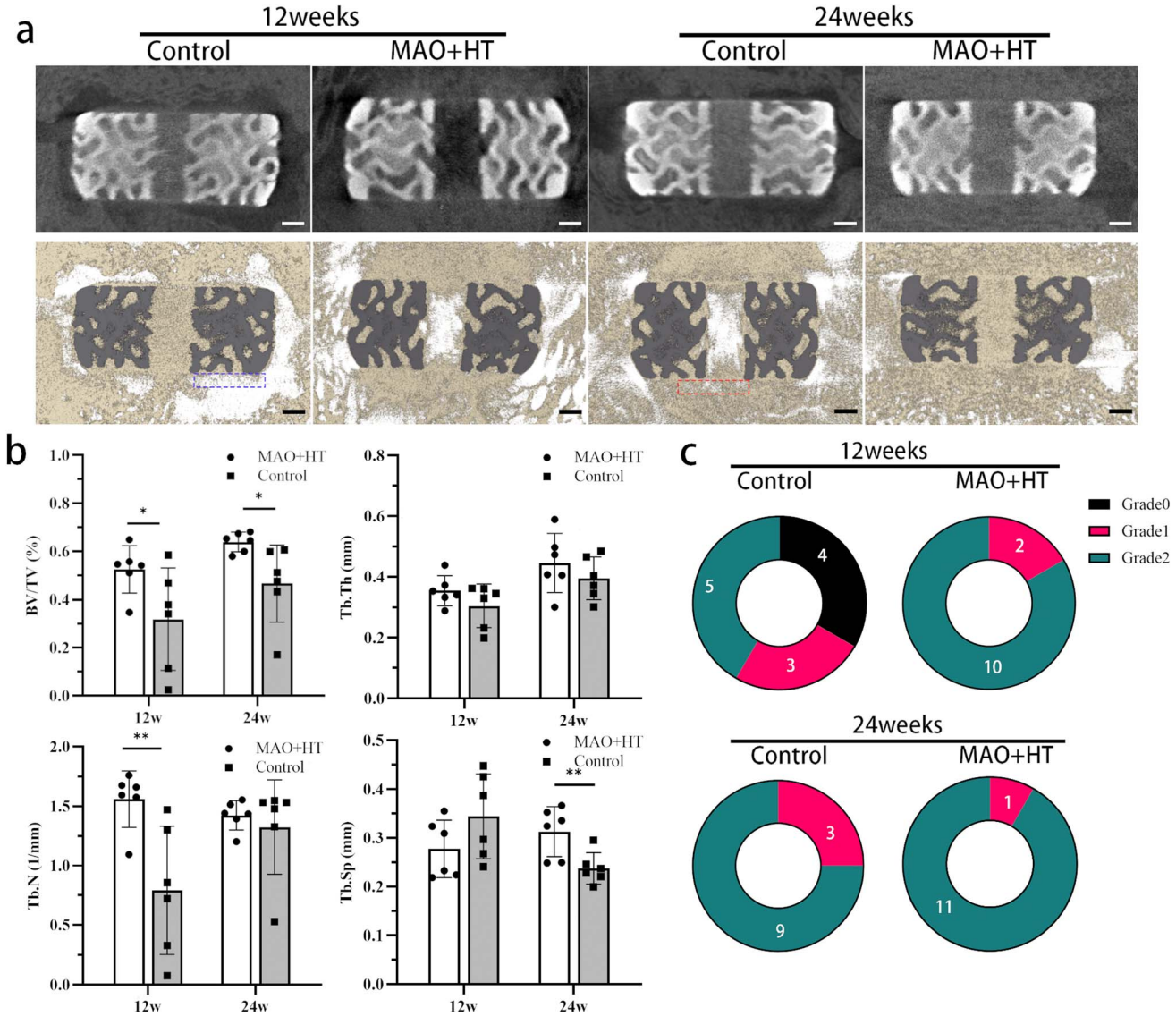

Fig. 3 Imaging reconstruction and analysis: (a) representative 2D and 3D micro-CT images of cages and the upper and lower endplates at 12 and 24 weeks after surgery; (b) quantitative analyses of trabecular bone volume fraction (BV/TV), trabecular thickness (Tb.Th), trabecular number (Tb.N), and trabecular separation (Tb.Sp) for ROI described above; (c) classification and induction of intervertebral fusion status according to our criteria, the size bar represents 1 mm.

shown in Fig. 3a. At 12 weeks, microcomputed tomography results showed evidence of compact peri-implant new bone formation in vast majority of intervertebral spaces in MAO + HT group without light transmission area around the cages. In contrast, certain gaps clearly existed between the cages and endplates in some cases in the untreated group indicated bone resorption and at same time point (blue box in Fig. 3a). At 24 weeks, an improvement in fusion rate was observed in both groups, such as the formation of bone bridges in the untreated group (red box in Fig. 3a) and sustaining bone union and bone remodeling around the cages in the MAO + HT group. Based on our criteria, there were 4 cases of no fusion, 3 cases of partial fusion and 5 cases of full fusion in untreated group, while no case of no fusion, 2 cases of partial fusion and 10 cases of full fusion in MAO + HT group at 12 weeks (Fig. 3c). MAO + HT group showed significantly high BV/TV values than those of control at 12 and 24 weeks (0.52 ± 0.97 verse 0.31 ± 0.20, 0.64 ± 0.38 verse 0.47 ± 0.17, $p < 0.05$), as well as higher Tb.N at 12 weeks (1.56 ± 0.24 verse 0.79 ± 0.54, $p < 0.01$), which further confirmed that MAO + HT coating could promote osteogenic activity in particular in the early stage (Fig. 3b).

3.2.2. Histological evaluation of tissue hard-tissue slices. Firstly, fluorescence labelling revealing the different osseointegration directions of the two groups (Fig. 4a). For both groups, the bone tissue grew from the surrounding host bone to the periphery of the cages (blue arrow in Fig. 4a). However, in addition to this, it could be observed that osseointegration directions from surface of the cages towards the adjacent endplate (white arrow in Fig. 4a) in MAO + HT group. Moreover, fluorescence signal of the newly generated bone was tightly adhered to the MAO + HT coating, while fibrous tissues were mostly observed in the same area in the untreated group. 10.38% higher mineral apposition rate (MAR) was also observed in MAO + HT group but did not reach the level of statistical significance in 12 weeks after surgery (Fig. 4b). The above differences decreased at 24 weeks after surgery.

Representative histological images of methylene blue acid fuchsin and modified Goldner trichrome staining of different groups are shown in Fig. 5. For the MAO + HT surface, more extensive and homogeneously distributed newly generated bone could be detected and gradually penetrated intra-porous region from 12 to 24 weeks (red triangle in Fig. 5a), indicating

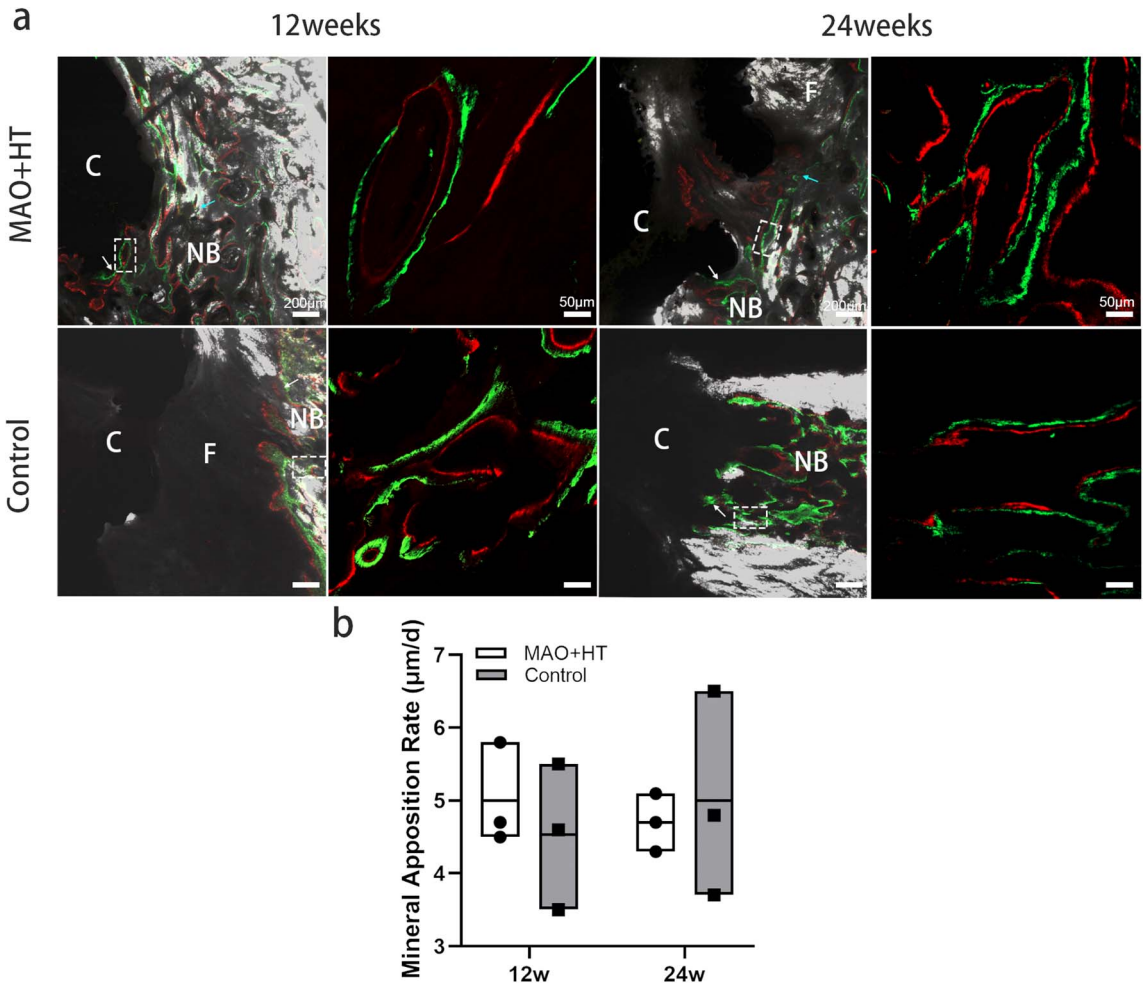

Fig. 4 Representative fluorescence imaging at 12 and 24 weeks after surgery: (a) region of endplate–cage interface labelled by calcein green and xylenol orange (b) the measurement of mineral apposition rate, C represents cage, F represents fibrous tissue, NB represents new bone, arrows indicate bone growth direction.

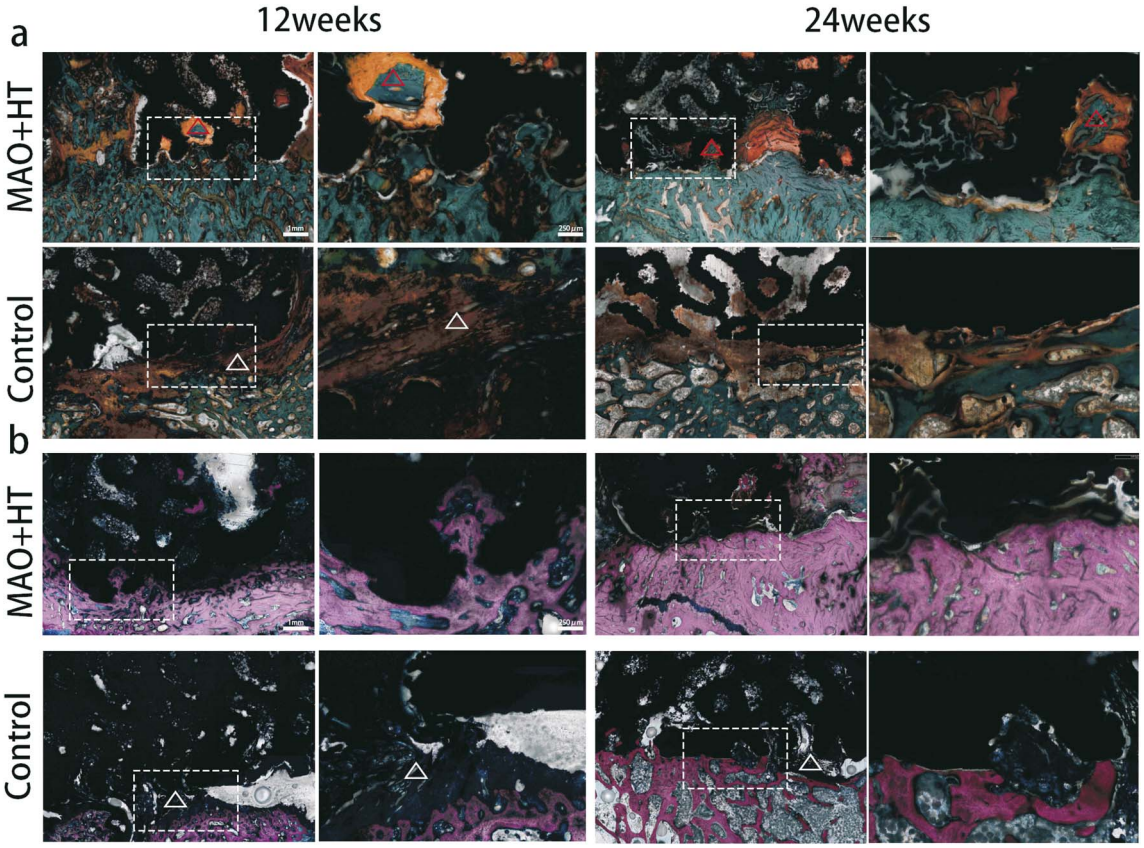

Fig. 5 Histomorphology analysis of the new formed tissue within the fusion zone between endplate and cage at 12 and 24 weeks. (a) Representative images of Goldner trichrome staining of the hard-tissue slices, black regions correspond to the cages, green color represents mineralized bone, orange color represents osteoid, brown color represents fibrous tissue, (b) representative images of methylene blue acid fuchsin staining of the hard-tissue slices, red color represents bone tissue, blue color represents fibrous tissue. Red triangle: bone tissue penetrated into intra-porous region, white triangle: fibrous tissue barrier.

a continuous ingrowth process. There was a direct contact between the MAO-HT cage implant and surrounding bone tissue. In contrast, bone trabeculae around the untreated cages were sparse, thin and exhibited ruptures. Moreover, fibrous tissue barrier between the untreated cage surface and native bone was commonly observed (white triangle in Fig. 5) just like fluorescence images, which showed an improvement at week 24.

3.2.3. Elements distribution of hard-tissue slices. The representative distribution of Ti, C, O Ca and P across the interface characterized by EDS was shown in Fig. 6. At 12 weeks, a Ca and P enrichment zone was detectable immediately adjacent to the MAO + HT coating, which indicated the presence of mineral, while no Ca, P enrichment was observed in corresponding area in control group. The aforementioned results were further confirmed by Line scan. Persistent Ca and P peaks appeared from 500 μm away from the MAO + HT Coating (red circle in Fig. 6a), however, the control group exhibited a certain degree of mineralization delay.

3.2.4. Biomechanical stability of implanted motion segments. To evaluate the biomechanical stability of spine fusion, the micro-motion between two vertebral bodies after the ACDF surgical intervention was quantified by the ROM assay. At 12 weeks, the average ROM values of MAO + HT and control group were 2.03 and 3.57 in loading modes of flexion–extension, however, the difference was not statistically significant attribute to the large dispersion of data. The differences between the treatment groups for lateral bending ROM were similar to that for flexion–extension, while the average axial rotation ROM was nearly identical between the groups (Fig. 7b). Two spinal motion segments were excluded from the experiment due to sample processing reasons. Differences of ROM for three different directions of motion were further narrowed at 24 weeks (Fig. 7b).

4 Discussion

In the current study, a high Ca/P ratio coating with hierarchical surface topography, which is similar to that of bone apatite, was successfully prepared on 3D printed titanium substrate through MAO and subsequent HT. Through the sheep ACDF model, we confirmed that the 3D printed Ti cage treated with MAO-HT technology could effectively promote interbody fusion and improve the motion stability of the cervical segments. MAO treatment could lead to a micron-scale topographical surface with numerous hemispheric rosette-like clumps. The

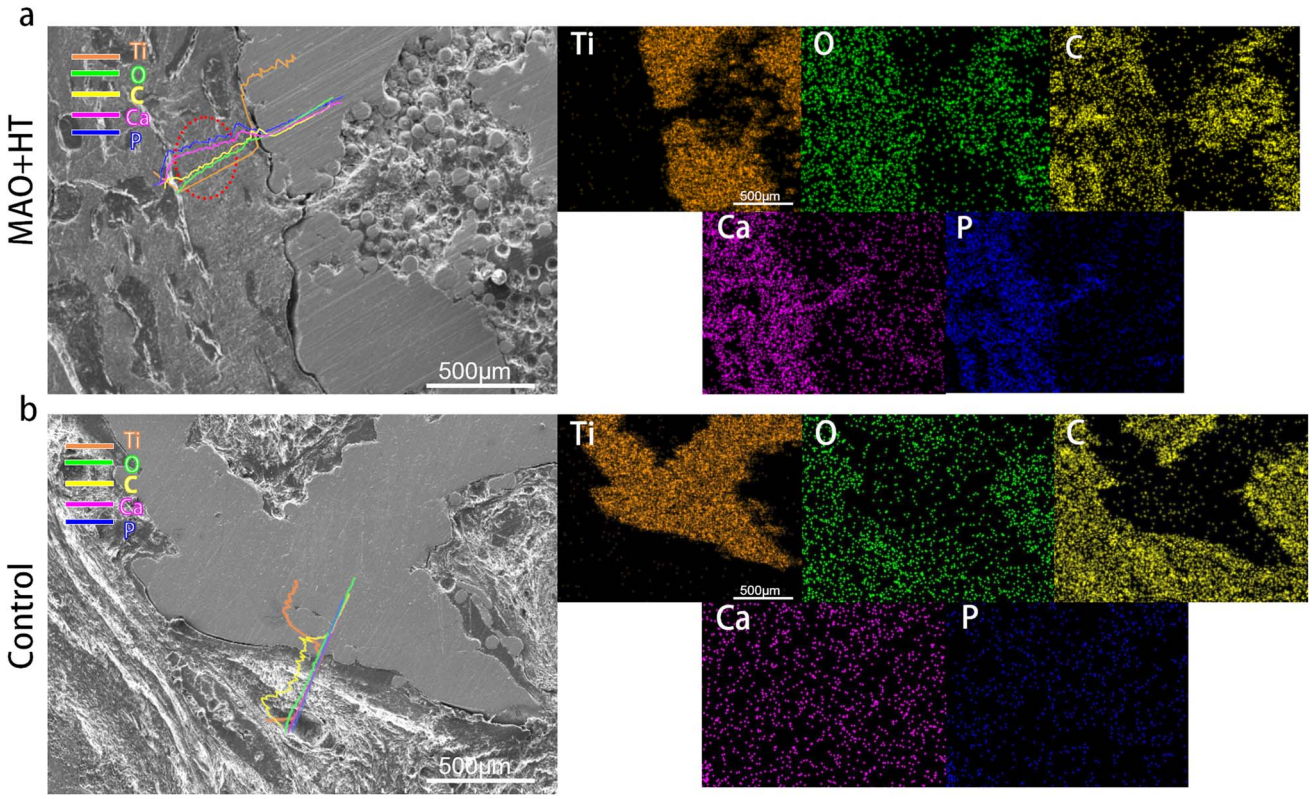

Fig. 6 EDS elemental map and line scan of Ti, C, O Ca and P across the endplate–cage interface at 12 weeks: (a) MAO + HT group; (b) untreated group.

subsequent HT process enables the *in situ* nucleation and growth of nano petals on MAO-fabricated surface. Using NaOH solution to perform hydrothermal treatment on titanium alloys helps to induce the formation of hydroxyapatite, thereby enhancing the bioactivity of titanium implants.[42] During the hydrothermal treatment, the following chemical reactions occur:[43]

TiO_2 oxide film reacts with OH^- as follows:

$$TiO_2 + OH^- \rightarrow HTiO^{3-} \quad (1)$$

Titanium further reacts with OH^-:

$$Ti + 3OH^- \rightarrow Ti(OH)_3^+ + 4e^- \quad (2)$$

$$Ti(OH)_3^+ + e^- \rightarrow TiO_2 \cdot H_2O + 1/2H_2\uparrow \quad (3)$$

$$Ti(OH)_3^+ + OH^- \leftrightarrow Ti(OH)_4 \quad (4)$$

Hydrated TiO_2 will continue to react with OH^-:

$$TiO_2 \cdot nH_2O + OH^- \leftrightarrow HTiO_3^- \cdot nH_2O \quad (5)$$

As a result, negatively charged hydrates form on the substrate surface, which can attract sodium ions from the solution through electrostatic interactions to form a sodium titanate hydrogel layer. The sodium ions in the hydrogel layer exchange with H_3O^+ in the aqueous solution, leading to an increase in the pH value on the substrate surface. The increase in pH enhances the ionic activity of hydroxyapatite, promoting its nucleation.[44] During the hydrothermal reaction, calcium ions and phosphate ions in the film layer diffuse outward under the influence of the hydrothermal medium, forming a locally supersaturated region of calcium and phosphate ions on the film surface. These calcium and phosphate ions react with hydroxide ions in the hydrothermal medium to produce hydroxyapatite. The reaction equation is as follows:

$$10Ca^{2+} + 6PO_4^{3-} + 2OH^- \rightarrow Ca_{10}(PO_4)_6(OH)_2 \quad (6)$$

During the bone remolding stage of the spine fusion, osteoclasts acidify the mineralized matrix, dissolving calcium phosphate crystals and creating microscale resorption lacunae (30–100 μm in diameter), and leave the collagen tufts and fibers as scaffolds at the submicro- and nanoscale.[14] Similar characteristically complex topology of 3D printed titanium alloys treated with MAO-HT can be recognized by osteoblasts then facilitate subsequent osseointegration.[45] Meanwhile, a robust interlock between the bone matrix and sub-micron topographical surface structures can be indicated by the non-collagenous proteins matrix secreted by the differentiating osteoblasts called "the cement line".[46]

Since the surface is the only region in contact with host bone tissue initially, surface characteristics are widely implicated in regulating several biological events that determine the

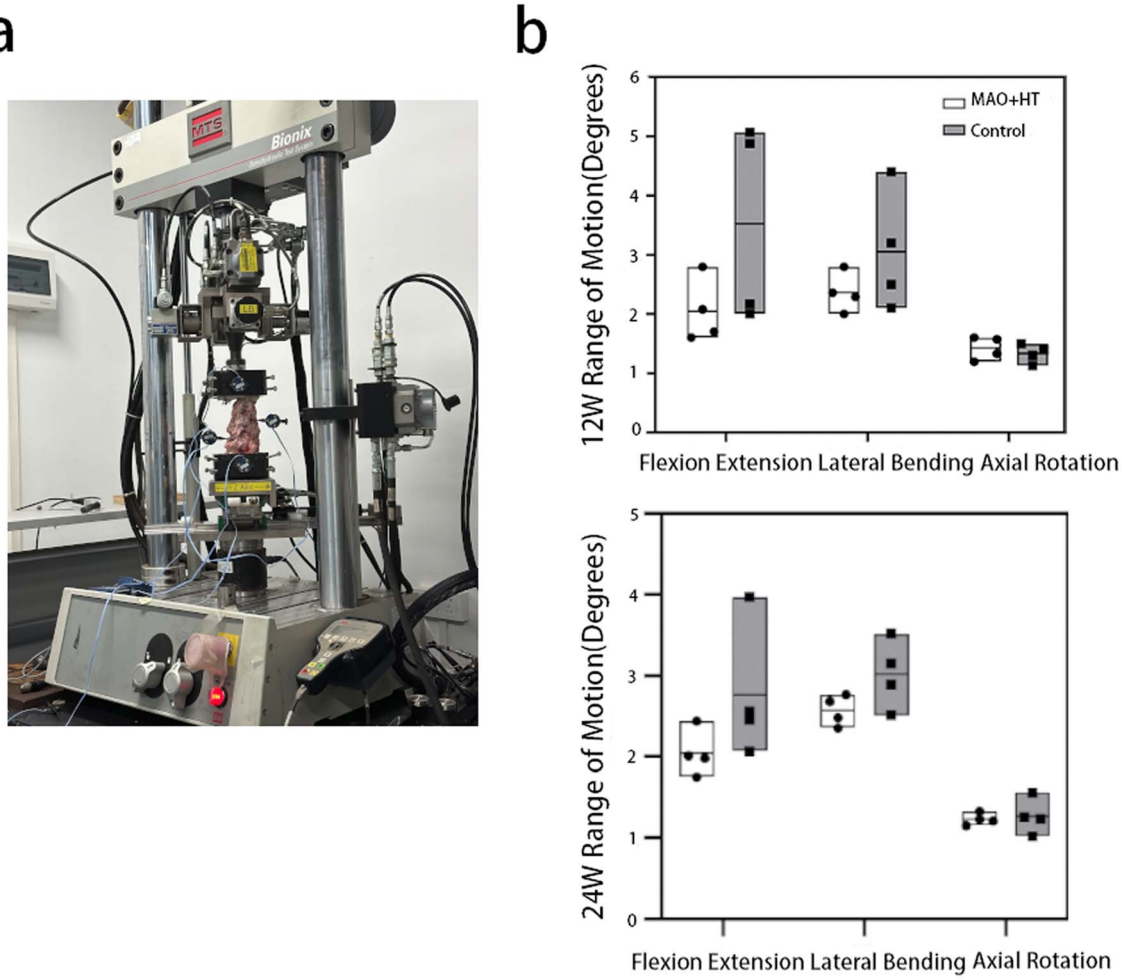

Fig. 7 Biomechanical analysis: (a) spinal motion segments fixed with 3D movement measuring system *via* cement; (b) range of motion (ROM) data collected for each loading mode.

mechanical stability and osseointegration outcome of the implant.[47] Meanwhile, microscopic morphology plays an important role in preventing a chronic immune response as well as regulating cell behaviors like attachment and differentiation. For example, Navarrete *et al.* found that NHOst and hMSCs cells seeded on surfaces with various topography characteristics displayed different integrin subunit expression, alkaline phosphatase activity and osteocalcin content,[48] suggesting that osteoblast lineage cells are sensitive to specific micro/nanostructures. In the present study, an evenly distributed crater-like porous structure with various pore sizes in microscale along with significantly different unique nano hemispheric rosette-like "clumps" structures in nanoscale after MAO + HT treatment was proved to promote the adhesion and proliferation of hBMSCs *in vitro* (Fig. 2). Meanwhile, higher degree of osteogenic differentiation of hBMSCs seeded on MAO + HT surface is demonstrated by increased ALP activity which is high in mineralized tissue cells and is considered to be an early marker of osteogenic differentiation. Surface wettability also take part in the regulation of classically activated (M1) macrophages and anti-inflammatory (M2) to maintain the balance of wound clearance and regeneration in bone repair. Meanwhile, the increased surface wettability combined with suitable nanostructures leading to continuous protein adsorption and the formation of a blood clot and fibrin network on the implant surface,[49] which is conducive to the adhesion and differentiation of osteogenesis-related cells.[50] Through the water contact angle experiment, it is proved that hydrothermal treatment can further improve the hydrophilicity of titanium alloy surface after MAO, providing a more appropriate active interface for bone repair (ESI Table 1†).

Interbody cage and internal fixation system play a major role in limiting motion and load bearing in the early postoperative period. Over time, along with the bone absorption and remodeling, a fusion mass forms in intervertebral space and load is transmitted through the newly formed bone.[12] The lack of interlock between interbody cages and host bone generates a vicious cycle that starts with micromotion and inflammation and ends with thickening of the fibrous layer, surrounding bone resorption and loosening of the cage.[14] Anteroposterior migration of the cage may lead to progressive spinal deformity and narrowing of the disc space, even mechanical compression and

secondary damage of spinal canal or foramen in some serious cases.[51] While, subsidence of an interbody cage into the vertebral body can lead to loss of indirect decompression and recurrence of neural compression.

In this experiment, no significant interbody cage migration or subsidence was detected in both groups. However, the vicious cycle mentioned above was founded in untreated group which trigger deterioration of stability in flexion, lateral bending directions (Fig. 5 and 7).

As we know, the mechanical property of the connection between the implant and the bone is one of the important parameters to determine the stability of implant. The stiffness of bone–implant interface changes along with the process of new bone formation that originated from the implant surface (so called contact osteogenesis) and the other from the pre-existing host bone (so called distance osteogenesis).[52,53] It has been demonstrated that contact osteogenesis is significantly faster than distance osteogenesis. More in detail, there is an open gap between the front of contact osteogenesis and distance osteogenesis during early stage of bone repair (days 0–30), resulting in low bone–implant interface stiffness constant around 1.87 GPa. It was not until the open gap closed (days 50) that the stiffness of the material begins to significantly increase, reaching 25 GPa, close to mature bone (days 100).[52] Thanks to the favourable cytocompatibility and osteogenic properties (Fig. 2), we found both contact osteogenesis and distance osteogenesis within the bone–MAO + HT cages interface, while in the case of smooth cage surfaces only distance osteogenesis was observed (Fig. 4a). It is easy to infer that the open gap existed within bone–untreated cage interface will result in micromotions between the cage and endplate, leading to decreased bonding strength and increased risk of fusion failure. And the bone–MAO + HT cages interface achieves stable mechanical strength in a relatively short period of time due to early contact of the osteogenic front ends in both directions.

Variations in trabecular bone architecture have been known to reflect mechanical quality of interbody fusions during the fusion process. As reported by Theo *et al.*, a more coarser and homogeneous bone structure was observed in "mature" spinal fusions characterized by increase in BV/TV ratio and Tb.Sp.[54] In line with this theory, similar changes in parameters of trabecular bone from 12 to 24 weeks of MAO + HT group compared with the control indicate a high-quality fusion mass (Fig. 3b).

According to the EDS elemental map, a widely extended calcium- and phosphorus-rich layer was detected between the MAO + HT cages and bone, but not in untreated group (Fig. 6). Previous reports reveal that CaP on the surface may link bony tissue to the implants *via* chemical bonding thereby accelerating the process of bone–implant bonding, resulting in more rapid and firmer mechanically interlock.[55] Furthermore, this thick calcium- and phosphorus-rich layer helps strengthen the vertebral endplate, which is particularly meaningful for osteoporotic patients. A single-center cohort study of 3D printed Ti cage subsidence for 55 patients showed that 8.2% of the vertebral bodies were found to have collapsed by more than 20% volume, and poor bone quality was considered as one of the most statistically significant risk factors.[56] Similarly, Okano *et al.* reported that vertebral bodies with lower endplate volumetric bone mineral density were prone to severe subsidence.[57] Thus, though not happened in sheep model, more mature and thicker mineralized bone surrounding the MAO + HT cages may reduce the risk of long-term cage subsidence in human.

The principal limitation of the study is that we only validated the performance of one type of MAO + HT treated 3D printed interbody cage with certain surface chemical composition and morphological characteristics in sheep ACDF model. Theoretically, a series of fusion cages with different morphological characteristics and chemical components should be developed by adjusting the electrolyte ratio, voltage and other reaction conditions for *in vivo* evaluation, so as to summarize the interaction between the repair tissue and the device surface characteristics, which might be different from the bone defect model and is specific to the biomechanics and osteogenic microenvironment of the intervertebral space mentioned above. This follow-up work is currently underway until the most suitable 3D printing interbody cage surface treatment completed by clinical validation.

5 Conclusion

In this study, a bioactive CaP coating with micro/nano multi-level morphology was developed on MAO + HT treated 3D printed Ti6Al4V. This coating helped to enhance the hydrophilicity, cell compatibility, and cell adhesion of hBMSCs on the material surface *in vitro*. Meanwhile, a tendency of higher expression of the osteogenic marker ALP suggested a possible early osteogenic commitment for MAO + HT group. In sheep ADCF model, compared with the untreated group, there were more direct contact and better fusion between the MAO + HT treated 3D interbody cage and surrounding bone tissue in the intervertebral space. Meanwhile, the better flexion–extension and lateral bending stability of the implanted segment at 12 weeks indirectly verified the promoting effect of the surface treated interbody cage on early fusion. The limitation of this study is the lack of a control group that only applies MAO or HT to identify the specific biological activity differences of each technology. However, despite the large differences between physiological and biomechanical environments, this study confirms that similar to the bone defect model, appropriate MAO + HT treatment can significantly promote bone repair in the interbody fusion. This discovery prompts us to develop more technologies and reaction parameters to find the optimal surface treatment scheme for clinical fusion devices.

Abbreviations

MAO	Microarc oxidation
HT	Hydrothermal treatment
CLSM	Confocal laser scanning microscope
ACDF	Anterior cervical discectomy and fusion
SEM	Scanning electron microscopy
XRD	X-ray diffraction
XPS	X-ray photoelectron spectroscopy

EDS	Energy dispersive spectrometer
ROI	Region of interest

Ethical statement

All experimental designs and protocols involving animals were approved by the Animal Ethics Committee Peking University Institutional Review Board Office (LA2022558) and complied with the recommendations of the academy's animal research guidelines.

Data availability

The data supporting this article have been included as part of the ESI.†

Author contributions

Jiang Sun: investigation, data curation, writing – original draft. Shan-Shan Liu: investigation, data curation. Da Zou: writing – review & editing. Ren-Hua Ni: data curation. Cong-Bin Wei: resources. Hao Wang: resources. Wei-Shi Li: writing – review & editing.

Conflicts of interest

The patent for the surface treatment technology used in the study was vested in Beijing AKec Medical Co., Ltd. The authors Chong-Bin Wei and Hao Wang work for the company. No financial support for the study was provided by the company. No other author has reported a potential conflict of interest relevant to this article.

Acknowledgements

This work was supported by the Research and Application of Clinical Diagnosis and Treatment Technology Foundation of Beijing (Grant No. Z201100005520073).

References

1 S. Jain, A. E. Eltorai, R. Ruttiman and A. H. Daniels, *Orthop. Surg.*, 2016, **8**, 278–284.
2 C. D. Lopez, V. Boddapati, J. M. Lombardi, N. J. Lee, C. Saifi, M. D. Dyrszka, Z. M. Sardar, L. G. Lenke and R. A. Lehman, *Spine J.*, 2020, **20**, 1586–1594.
3 C. Q. Jia, Z. Zhang, S. Q. Cao, T. J. Wang, H. C. Yu, W. X. Wang, B. M. Guo, X. Y. Qiu, Y. G. You, F. Q. Hu, J. Zhao and X. S. Zhang, *Bioact. Mater.*, 2023, **23**, 234–246.
4 G. W. Bagby, *Orthopedics*, 1988, **11**, 931–934.
5 J. R. Dimar, S. D. Glassman, K. J. Burkus and L. Y. Carreon, *Spine*, 2006, **31**, 2534–2539; discussion 2540.
6 M. R. Van Horn, R. Beard, W. Wang, B. W. Cunningham, K. P. Mullinix, M. Allall and B. S. Bucklen, *Spine J.*, 2021, **21**, 2097–2103.
7 G. Fogel, N. Martin, K. Lynch, M. H. Pelletier, D. Wills, T. Wang, W. R. Walsh, G. M. Williams, J. Malik, Y. Peng and M. Jekir, *Spine J.*, 2022, **22**, 1028–1037.
8 P. Li, W. Jiang, J. Yan, K. Hu, Z. Han, B. Wang, Y. Zhao, G. Cui, Z. Wang, K. Mao, Y. Wang and F. Cui, *J. Biomed. Mater. Res., Part A*, 2019, **107**, 1386–1392.
9 K. C. McGilvray, J. Easley, H. B. Seim, D. Regan, S. H. Berven, W. K. Hsu, T. E. Mroz and C. M. Puttlitz, *Spine J.*, 2018, **18**, 1250–1260.
10 T. Makino, S. Takenaka, Y. Sakai, H. Yoshikawa and T. Kaito, *Global Spine J.*, 2022, **12**, 931–939.
11 P. M. Beck, *Oral Health*, 1970, **60**, 19–21 passim.
12 P. J. Rao, M. H. Pelletier, W. R. Walsh and R. J. Mobbs, *Orthop. Surg.*, 2014, **6**, 81–89.
13 W. Liu, X. Li, Y. Jiao, C. Wu, S. Guo, X. Xiao, X. Wei, J. Wu, P. Gao, N. Wang, Y. Lu, Z. Tang, Q. Zhao, J. Zhang, Y. Tang, L. Shi and Z. Guo, *ACS Appl. Mater. Interfaces*, 2020, **12**, 51885–51903.
14 R. A. Gittens, R. Olivares-Navarrete, Z. Schwartz and B. D. Boyan, *Acta Biomater.*, 2014, **10**, 3363–3371.
15 T. Zhang, W. Zhou, Z. Jia, Q. Wei, D. Fan, J. Yan, C. Yin, Y. Cheng, H. Cai, X. Liu, H. Zhou, X. Yang, Y. Zheng and Z. Liu, *Sci. China Mater.*, 2018, **61**, 579–592.
16 S. Amin Yavari, J. van der Stok, Y. C. Chai, R. Wauthle, Z. Tahmasebi Birgani, P. Habibovic, M. Mulier, J. Schrooten, H. Weinans and A. A. Zadpoor, *Biomaterials*, 2014, **35**, 6172–6181.
17 H. Lee, T.-S. Jang, J. Song, H.-E. Kim and H.-D. Jung, *Mater. Lett.*, 2016, **185**, 21–24.
18 M. A. Lopez-Heredia, J. Sohier, C. Gaillard, S. Quillard, M. Dorget and P. Layrolle, *Biomaterials*, 2008, **29**, 2608–2615.
19 P. Xiu, Z. Jia, J. Lv, C. Yin, Y. Cheng, K. Zhang, C. Song, H. Leng, Y. Zheng, H. Cai and Z. Liu, *ACS Appl. Mater. Interfaces*, 2016, **8**, 17964–17975.
20 J. C. M. Souza, M. B. Sordi, M. Kanazawa, S. Ravindran, B. Henriques, F. S. Silva, C. Aparicio and L. F. Cooper, *Acta Biomater.*, 2019, **94**, 112–131.
21 S. Sikdar, P. V. Menezes, R. Maccione, T. Jacob and P. L. Menezes, *Nanomaterials*, 2021, **11**, 1375.
22 Q. Du, D. Q. Wei, S. D. Wang, S. Cheng, Y. M. Wang, B. Q. Li, D. C. Jia and Y. Zhou, *Appl. Surf. Sci.*, 2019, **487**, 708–718.
23 Y. Han, J. H. Zhou, S. M. Lu and L. Zhang, *RSC Adv.*, 2013, **3**, 11169–11184.
24 H.-J. Song, J.-W. Kim, M.-S. Kook, W.-J. Moon and Y.-J. Park, *Appl. Surf. Sci.*, 2010, **256**, 7056–7061.
25 Y. Li, W. Wang, F. Yu, D. Wang, S. Guan, Y. Li and M. Qi, *Mater. Sci. Eng., C*, 2020, **109**, 110610.
26 H.-J. Song, K.-H. Shin, M.-S. Kook, H.-K. Oh and Y.-J. Park, *Surf. Coat. Technol.*, 2010, **204**, 2273–2278.
27 G. Li, H. Cao, W. Zhang, X. Ding, G. Yang, Y. Qiao, X. Liu and X. Jiang, *ACS Appl. Mater. Interfaces*, 2016, **8**, 3840–3852.
28 G. L. Zhao, L. Xia, B. Zhong, S. S. Wu, L. Song and G. W. Wen, *Trans. Nonferrous Met. Soc. China*, 2015, **25**, 1151–1157.
29 P. L. Jiang, J. H. Liang and C. J. Lin, *Appl. Surf. Sci.*, 2013, **280**, 373–380.
30 W. Shang, B. Chen, X. Shi and Y. Wen, *Chin. J. Mater. Res.*, 2011, **25**, 57–60.

31 P. Shi, W. F. Ng, M. H. Wong and F. T. Cheng, *J. Alloys Compd.*, 2009, **469**, 286–292.
32 W. Zhang, G. Wang, Y. Liu, X. Zhao, D. Zou, C. Zhu, Y. Jin, Q. Huang, J. Sun, X. Liu, X. Jiang and H. Zreiqat, *Biomaterials*, 2013, **34**, 3184–3195.
33 X. Shen, Y. Zhang, P. Ma, L. Sutrisno, Z. Luo, Y. Hu, Y. Yu, B. Tao, C. Li and K. Cai, *Biomaterials*, 2019, **212**, 1–16.
34 Y. Zhao, H. Cao, H. Qin, T. Cheng, S. Qian, M. Cheng, X. Peng, J. Wang, Y. Zhang, G. Jin, X. Zhang, X. Liu and P. K. Chu, *ACS Appl. Mater. Interfaces*, 2015, **7**, 17826–17836.
35 I. A. J. van Hengel, M. Lacin, M. Minneboo, L. E. Fratila-Apachitei, I. Apachitei and A. A. Zadpoor, *Mater. Sci. Eng., C*, 2021, **124**, 112074.
36 Q. Huang, X. Liu, T. A. Elkhooly, R. Zhang, Z. Shen and Q. Feng, *Colloids Surf., B*, 2015, **134**, 169–177.
37 N. Newell, J. P. Little, A. Christou, M. A. Adams, C. J. Adam and S. D. Masouros, *J. Mech. Behav. Biomed. Mater.*, 2017, **69**, 420–434.
38 H. Xu, F. Zhang, H. Wang, F. Geng, M. Shao, S. Xu, X. Xia, X. Ma, F. Lu and J. Jiang, *BioMed Res. Int.*, 2018, **2018**, 7961509.
39 Y. Hojo, Y. Kotani, M. Ito, K. Abumi, T. Kadosawa, Y. Shikinami and A. Minami, *Biomaterials*, 2005, **26**, 2643–2651.
40 T. Zhang, Q. Wei, D. Fan, X. Liu, W. Li, C. Song, Y. Tian, H. Cai, Y. Zheng and Z. Liu, *Biomater. Sci.*, 2020, **8**, 1279–1289.
41 S. Wang, H. Leng, Y. Tian, N. Xu and Z. Liu, *BMC Musculoskeletal Disord.*, 2021, **22**, 121.
42 L. Huang, B. Cai, Y. Huang, J. Wang, C. Zhu, K. Shi, Y. Song, G. Feng, L. Liu and L. Zhang, *ACS Omega*, 2021, **6**, 1465–1476.
43 H. M. Kim, F. Miyaji, T. Kokubo and T. Nakamura, *J. Biomed. Mater. Res.*, 1996, **32**, 409–417.
44 T. Kokubo, H. M. Kim and M. Kawashita, *Biomaterials*, 2003, **24**, 2161–2175.
45 R. J. McMurray, N. Gadegaard, P. M. Tsimbouri, K. V. Burgess, L. E. McNamara, R. Tare, K. Murawski, E. Kingham, R. O. C. Oreffo and M. J. Dalby, *Nat. Mater.*, 2011, **10**, 637–644.
46 J. E. Davies, E. Ajami, R. Moineddin and V. C. Mendes, *Biomaterials*, 2013, **34**, 3535–3546.
47 R. Agarwal and A. J. Garcia, *Adv. Drug Delivery Rev.*, 2015, **94**, 53–62.
48 R. Olivares-Navarrete, S. L. Hyzy, M. E. Berg, J. M. Schneider, K. Hotchkiss, Z. Schwartz and B. D. Boyan, *Ann. Biomed. Eng.*, 2014, **42**, 2551–2561.
49 B. S. Kopf, S. Ruch, S. Berner, N. D. Spencer and K. Maniura-Weber, *J. Biomed. Mater. Res., Part A*, 2015, **103**, 2661–2672.
50 K. M. Hotchkiss, G. B. Reddy, S. L. Hyzy, Z. Schwartz, B. D. Boyan and R. Olivares-Navarrete, *Acta Biomater.*, 2016, **31**, 425–434.
51 M. K. Park, K. T. Kim, W. S. Bang, D. C. Cho, J. K. Sung, Y. S. Lee, C. K. Lee, C. H. Kim, B. K. Kwon, W. K. Lee and I. Han, *Spine J.*, 2019, **19**, 437–447.
52 S. Gershov, J. Xie, F. A. Shah, K. Shemtov-Yona and D. Rittel, *Acta Biomater.*, 2022, **154**, 302–311.
53 N. Amor, L. Geris, J. Vander Sloten and H. Van Oosterwyck, *Acta Biomater.*, 2011, **7**, 779–790.
54 T. H. Smit, R. Müller, M. van Dijk and P. I. Wuisman, *Spine*, 2003, **28**, 1802–1808; discussion 1809.
55 Z. M. Huang, Y. Y. Qi, S. H. Du, G. Feng, H. Unuma and W. Q. Yan, *Sci. Technol. Adv. Mater.*, 2013, **14**, 055001.
56 H. Wu, Z. Shan, F. Zhao and J. P. Y. Cheung, *Clin. Orthop. Relat. Res.*, 2022, **480**, 163–188.
57 I. Okano, C. Jones, S. N. Salzmann, M. J. Reisener, O. C. Sax, C. Rentenberger, J. Shue, J. A. Carrino, A. A. Sama, F. P. Cammisa, F. P. Girardi and A. P. Hughes, *Eur. Spine J.*, 2020, **29**, 1131–1140.